

# Solidification Behavior and Microstructure Evolution in Dissimilar Electron Beam Welds Between Commercially Pure Iron and Nickel



JORIS HOCHANADEL, BOYD PANTON, CAROLIN FINK, and JOHN LIPPOLD

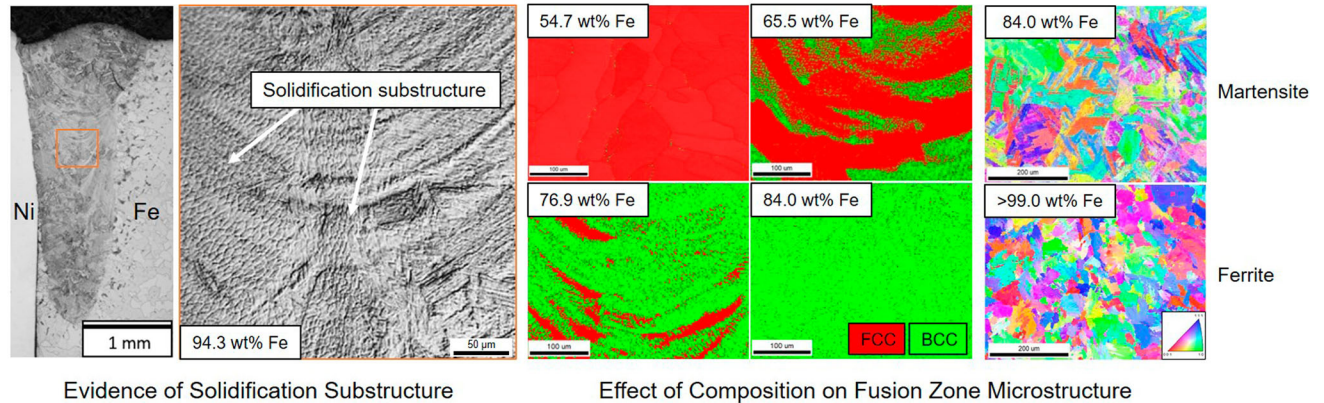
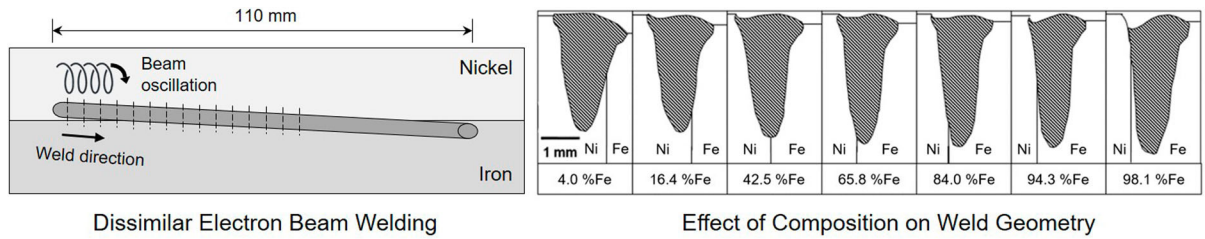
Electron beam welding processes have highly accurate control of both spatial and temporal heating profiles which provide unique capabilities in dissimilar metals joining. In this work, electron beam welds were made between commercially pure nickel and iron to determine the effect of fusion zone composition on solidification behavior and microstructure evolution. The weld was made with a beam deflected in a circular pattern to enable joining and promote mixing. The beam traveled at a shallow angle of approximately 1 deg to the joint interface starting in the nickel and finishing in the iron. The shallow angle created a weld with a composition gradient along its 110 mm length. The solidification behavior and final weld microstructure were characterized using both light optical microscopy and scanning electron microscopy. Electron backscatter diffraction was used to determine the phase fractions in the fusion zone. A change in solidification mode from face-centered cubic austenite to body-centered cubic ferrite was observed as a function of fusion zone composition. Weld cross-sections containing 65.5 wt pct Fe and 76.9 wt pct Fe had a two-phase fcc + bcc microstructure. Using the compositions and phase fractions, the two-phase region was estimated to be between 56.4 and 79.7 wt pct Fe. Martensite was observed in cross-sections containing between 76.9 wt pct Fe and 98.1 wt pct Fe, which was confirmed using hardness measurements.

---

JORIS HOCHANADEL, BOYD PANTON, CAROLIN FINK, and JOHN LIPPOLD are with the Department of Materials Science and Engineering, The Ohio State University, Columbus, OH 43221. Contact e-mail: hochanadel.4@osu.edu

Manuscript submitted November 2, 2023; accepted March 10, 2024.

Article published online March 27, 2024



<https://doi.org/10.1007/s11661-024-07375-y>  
 © The Author(s) 2024

### I. INTRODUCTION

ELECTRON beam welding (EBW) is used to produce high-quality, low heat input welds in a range of critical applications including power generation, aerospace, and semiconductor manufacturing.<sup>[1,2]</sup> The high cost of the EBW equipment means that there are relatively few publications on EBW and there are even

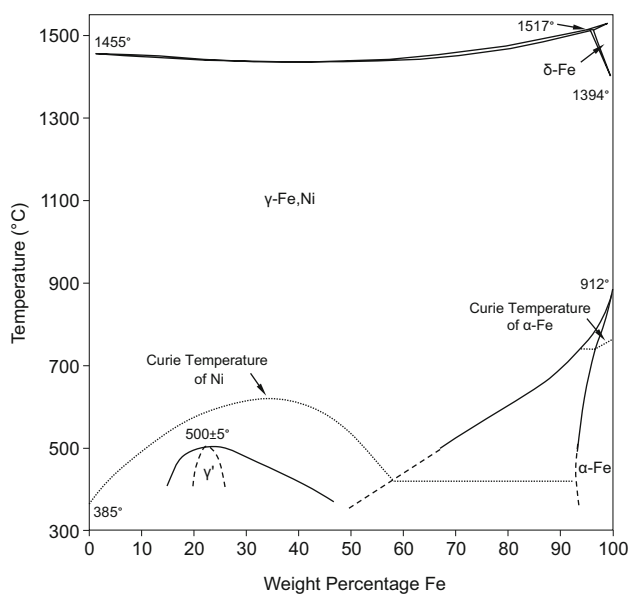


Fig. 1—Nickel-Iron binary phase diagram. Reproduced from Ref. [16].

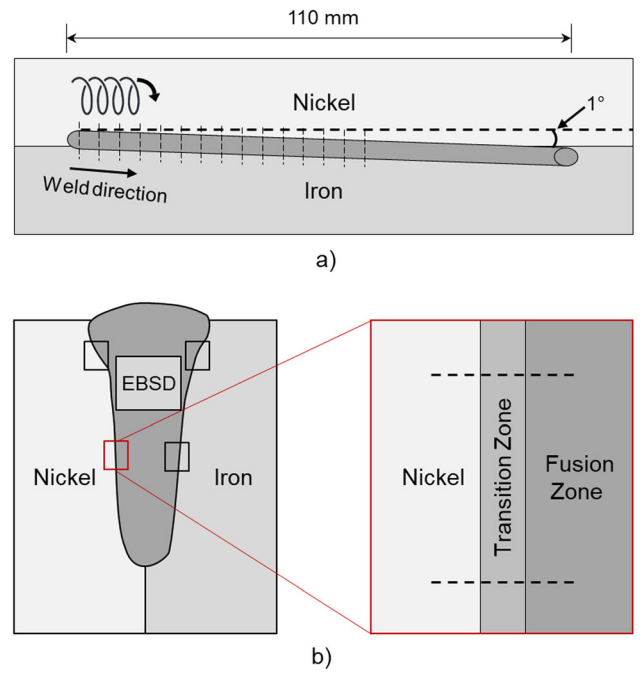


Fig. 2—(a) Schematic of electron beam weld (top view) from the nickel toward the iron. Arrows indicates direction of weld and beam deflection. Dashed lines indicate locations of weld cross-sections (at 4 mm intervals). Note 1 deg weld angle is for visualization only: not to scale. (b) Schematic of weld cross-section, indicating location of EDS and EBSD scans. Two EDS scans (dashed lines) were obtained across the transition zone on both the nickel and iron side.

fewer on EBW of dissimilar metals. This lack of literature impacts both the fundamental understanding of metallurgical phenomena associated with dissimilar EBW and the application of EBW for dissimilar metal joining. Previous investigations have laid the groundwork to determine the level of influence of process variables on the weld penetration and microstructure.<sup>[2–8]</sup> A limited number of papers have analyzed EBW of dissimilar metal welds. Common features associated with dissimilar EBW include incomplete mixing and high hardness regions along the weld interface.<sup>[9–12]</sup> Although beam deflection can be used for improved weld pool mixing,<sup>[9]</sup> microstructural morphologies and phases have been observed to differ at the dissimilar interface between the base metal and fusion zone.

There are many practical applications where face-centered cubic (fcc) metals are joined or clad onto body-centered cubic (bcc) metals. This is especially apparent when joining nickel-based alloys to steels for corrosive environments.<sup>[13–15]</sup> Many engineering alloys consist of iron–nickel systems, including alloy steels, stainless steels, and superalloys. These systems are used widely in dissimilar welding and cladding.<sup>[13–15]</sup> A phase diagram of the binary iron–nickel system is shown in Figure 1. Engineering alloys contain a range of elements that can affect the dynamics of solidification and subsequent microstructural evolution in the weld metal. The current study used pure iron (bcc) and nickel (fcc) to simplify the solidification conditions during EBW.

In dissimilar metal welding, control of dilution and mixing of the two materials is generally desired to ensure good weldability. Dissimilar welds often require control of dilution to form desirable microstructures or phases,<sup>[17]</sup> while cladding often requires minimization of dilution to avoid degradation of weld properties.<sup>[13]</sup> While the fusion zone composition is largely a homogeneous mixture of the two metals, dissimilar metal welds exhibit a sharp gradient in composition at the fusion boundary, referred to as a composition transition zone.<sup>[14]</sup> The transition zone is typically a narrow region (Figure 2(b)), but can be of critical importance for weld performance as the gradient in composition may result in undesirable microstructures or defect formation.<sup>[14]</sup> Numerous failure modes may occur in the transition zone including hydrogen cracking<sup>[13]</sup> or creep rupture from variations in creep strength.<sup>[14]</sup>

The objective of this work is to determine the effect of fusion zone composition on the solidification behavior and microstructural evolution in a dissimilar metal EBW weld between iron and nickel. Experiments were

designed to create welds at various dilutions to understand the influence of fusion zone composition on the weld geometry, and the weld microstructure evolution.

## II. EXPERIMENTAL PROCEDURES

Commercially pure iron and nickel were welded in a butt joint configuration using a pro-beam K10 high-voltage EBW machine. The iron was in the form of a circular forging with a diameter of 150 mm. Sections were cut from the forging with a nominal thickness of 5 mm. The nickel was in the form of a hot rolled plate with dimensions 75 × 120 × 6 mm. Prior to welding, these pieces were machined to remove mill scale and then cleaned with ethanol. The compositions of the plates are listed in Table I. Both parts were demagnetized using a surface-type demagnetizer and verified using a digital magnetic field detector. The parts were loaded to the same working height using a shim. Due to imperfections in the fixturing, the actual working height of the nickel plate was slightly higher during welding resulting in the difference in height between the Ni and Fe side observed in the weld cross-sections. Limited access to the EBW equipment prohibited the authors from a second trial to address this fixturing error. The chamber was pumped down to  $3 \times 10^{-4}$  torr ( $3.9 \times 10^{-7}$  atm), and a weld was made at an angle of approximately 1 deg to the joint, starting in the nickel and ending in the iron (Figure 2(a)). The weld was approximately 110 mm in length. Using a magnetic deflection lens, the electron beam was deflected, moving the heat source in a clockwise circular pattern with an amplitude of 0.5 mm and a frequency of 1000 Hz. This deflection is a standard technique performed to increase the size of the melt pool, therefore promoting fusion. It has been observed that at high frequencies, such as what was used in this study, the weld does not cause advancing or retreating sides observed at lower frequencies.<sup>[18]</sup> Fusion occurred from the beginning of the weld to 60 mm of weld length, after which there was a lack of significant fusion in the nickel. The lack of fusion was attributed to residual magnetism that caused the beam to deflect away from the joint into the iron. The beam was characterized prior to welding using a pro-beam diagnostic tool. This was done to determine the lens current and deflection current to be used. The welding parameters are listed in Table II.

The weld was cross-sectioned transverse to the welding direction at 4-mm intervals over the entire range of fusion (*i.e.*, a total of 15 weld cross-sections were prepared). The sections were cut perpendicular to the plate. Although the weld was made at an angle, the

**Table I. Composition of Plate Materials (in Wt Pct)**

Material	Fe	Ni	C	Si	Mn	Cu	S	P	Co
CP Iron	bal.	—	0.02	0.01	0.32	—	0.013	0.01	—
CP Nickel	0.02	bal.	0.01	0.05	0.23	0.01	< 0.001	—	< 0.01

**Table II. Electron Beam Welding Conditions**

Voltage	Beam Current	Travel Speed	Vacuum Level	Focus Condition	Deflection Amplitude	Deflection Frequency	Weld Angle
100 kV	12 mA	12 mm/s	$3 \times 10^{-4}$ torr	0.5 mm (over)	0.5 mm	1000 Hz	$\sim 1$ deg

difference in geometry measurement due to sectioning perpendicular to the plate is minimal since the angle was so shallow. Each section was ground, polished to  $1 \mu\text{m}$  and finished to  $0.05 \mu\text{m}$  using colloidal silica on a vibratory polisher. All sections were etched using 2 pct Nital (98 pct ethanol, 2 pct nitric acid). Some sections with significant austenite in the weld did not etch, so these sections were re-polished and etched using Kalling's II reagent (100 mL HCl, 100 mL ethanol, 5 g  $\text{CuCl}_2$ ). Each weld section was imaged with a light optical microscope (LOM). The bulk fusion zone composition for each weld cross-section was calculated using macro energy dispersive spectroscopy (EDS) maps. Multiple maps were taken at  $200\times$  magnification and stitched to encompass the whole weld. The maps used a voltage of 20 kV and a beam current of 3.2 nA. Each stitched map was then processed to select the weld fusion zone, and the average composition in the fusion zone was determined to be the bulk fusion zone composition. Although EDS is typically employed for qualitative as opposed to quantitative measurements, the results were checked using area pct measurements from photo-macrographs and lined up well. The EDS measurements only considered Fe and Ni measurements, which have been studied previously and are well understood.<sup>[19]</sup> Selected weld sections were examined with a scanning electron microscope (SEM) using EDS and electron backscatter diffraction (EBSD). The micro-EDS measurements were made to analyze the local composition in the fusion zone, in particular the composition gradient across the transition zone along the weld interface. These measurements used a voltage of 10 kV and a beam current of 6.4 nA. Two EDS line scans were performed at the top and middle of both the iron and nickel interface of each section (Figure 2(b)). EBSD maps at a voltage of 20 kV and a beam current of 32 nA with a step size of  $1 \mu\text{m}$  were taken to quantify phase fractions in the fusion zone microstructure for each weld section. A schematic of where EBSD analysis was performed is shown in Figure 2. When analyzing EBSD results, martensite will often be indexed as bcc. The body-centered tetragonal (bct) crystal structure of the martensitic phase is often erroneously indexed as bcc because the lattice distortion is typically very low. These low distortions result in diffraction patterns that are very close to bcc patterns. In low-carbon Fe–Ni martensite, this lattice distortion is even smaller, making it very difficult to distinguish.<sup>[20,21]</sup> Vickers hardness measurements using a load of 200 g were made along the top, middle, and bottom of weld cross-sections that were indexed containing some amount of bcc in EBSD to determine the presence of martensite. To estimate the cooling rate during solidification, 10 cell spacing

measurements were performed at each interface in the weld section containing 54.7 wt pct Fe.

### III. RESULTS AND DISCUSSION

#### A. Weld Geometry

Figure 3 illustrates the change in weld geometry as a function of bulk fusion zone composition. As previously described, cross-sections were taken at 4 mm increments. Note that there are a higher number of data points at high Fe content because the beam deflection associated with residual magnetism in the iron base plate caused to the weld to slightly deviate from the programmed trajectory, shifting it to the iron plate prematurely. Figures 3(a) and (b) show that as weight percent Fe increases in the fusion zone, the depth of weld penetration increases and the weld top width decreases. Half-penetration width (*i.e.*, the width of the fusion zone at half of the depth of penetration) and fusion zone area show little change as a function of composition (Figures 3(c) and (d)). Figure 3(e) depicts weld geometries extracted from the actual micrographs for better visualization.

There is a significant role of fusion zone composition on weld penetration (Figure 3(a)). The dominant material properties for the difference in the depth of penetration are vapor pressure, surface tension, and density of the material.<sup>[22,23]</sup> Rai *et al.*<sup>[3]</sup> show that vapor pressure allows the keyhole to remain open. This vapor pressure is dependent on the surface tension and hydrostatic force (which is related to density). This relationship follows the following equation:

$$p = \rho g z + \gamma(T)/r(z),$$

where  $p$  is the vapor pressure in the keyhole,  $\rho$  is the density,  $g$  is the acceleration due to gravity,  $z$  is the distance from the surface of the plate,  $\gamma(T)$  is the surface tension at a given temperature  $T$ , and  $r(z)$  is the keyhole radius at a given depth  $z$ . Although iron has a slightly lower vapor pressure at temperatures near melting relative to nickel, it has been shown that at elevated temperatures, iron will have a higher vapor pressure under vacuum conditions. At 2000 K and at a vacuum level of 0.01 Pa ( $9.9 \times 10^{-8}$  atm), iron has a vapor pressure of approximately  $1.7 \times 10^{-2}$  atm and nickel has a vapor pressure of approximately  $8.8 \times 10^{-3}$  atm, meaning vaporization can more readily occur in iron.<sup>[24]</sup> The surface tension is higher and density of iron is lower than nickel at 1600 °C. These material properties are summarized in Table III. Using these numbers in the equation above and assuming a keyhole radius of 1 mm

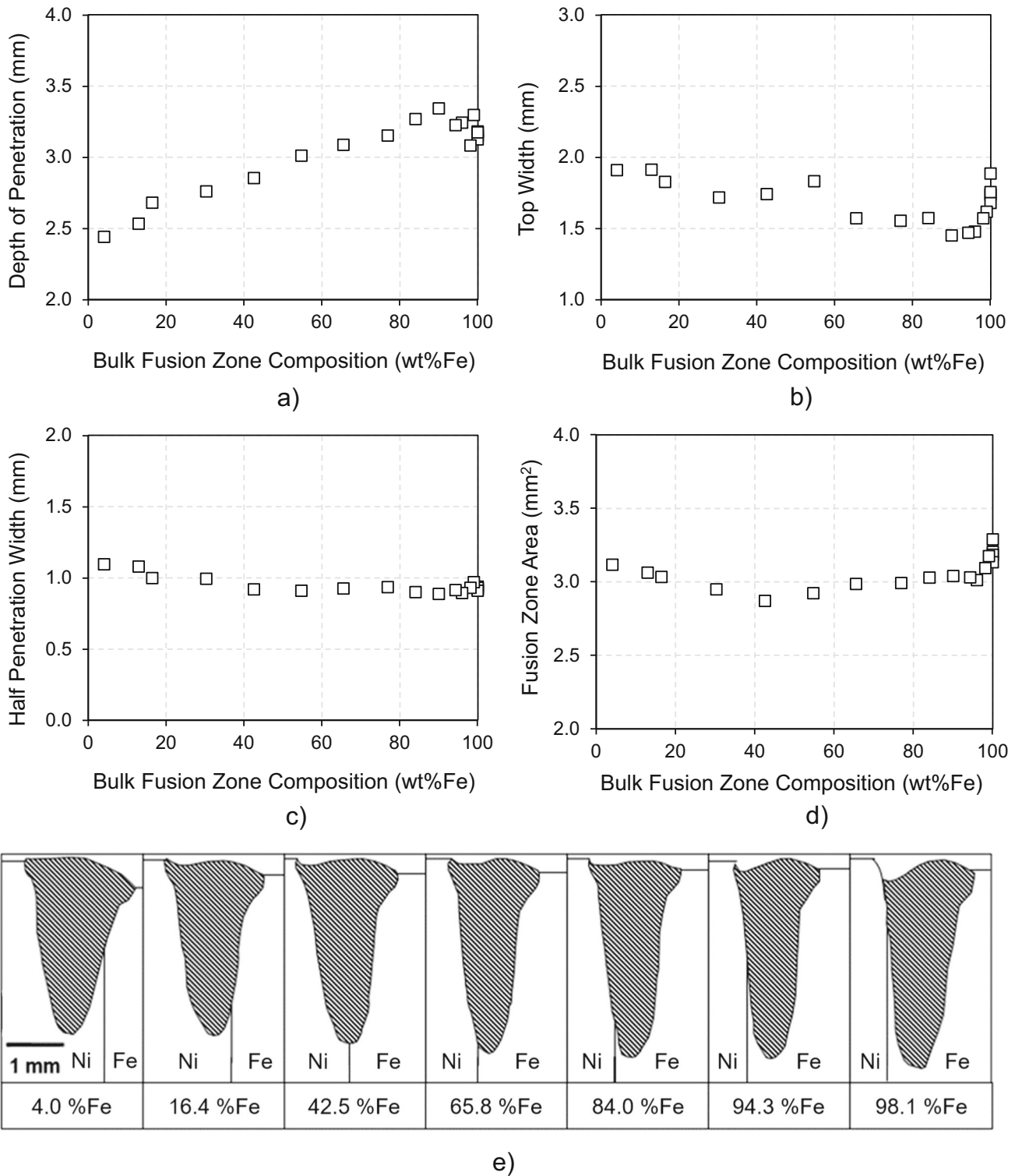


Fig. 3—Effect of bulk fusion zone composition on (a) depth of penetration, (b) weld top width, (c) half-penetration width, (d) and fusion zone area. (e) Weld cross-section contours extracted from actual micrographs at varying bulk fusion zone compositions, measured in wt pct Fe.

at a depth in the mm scale, the pressure in the keyhole with higher Fe content will be greater, allowing the keyhole to stay open. The surface tension of Fe–Ni alloys containing 75 at. pct Fe has been shown to be similar to 100 at. pct Fe.<sup>[25]</sup> Thus, the penetration at high

Fe content will level out, as can be seen in Figure 3(a). Inconsistencies in penetration at high Fe content are attributed to the dynamic nature of the keyhole. As noted, the half-penetration width does not change significantly throughout the weld (Figure 3(c)). This is

**Table III. Material Properties for Iron and Nickel**

	Melting Temperature (°C) <sup>[26]</sup>	Boiling Temperature (°C) <sup>[26]</sup>	Density $\rho$ at $\sim 1600$ °C (kg/m <sup>3</sup> ) <sup>[27,28]</sup>	Surface Tension $\gamma$ at 1600 °C (N/m) <sup>[23]</sup>
Fe	1536	2860	$\sim 6950$	1.9
Ni	1455	2915	$\sim 7500$	1.72

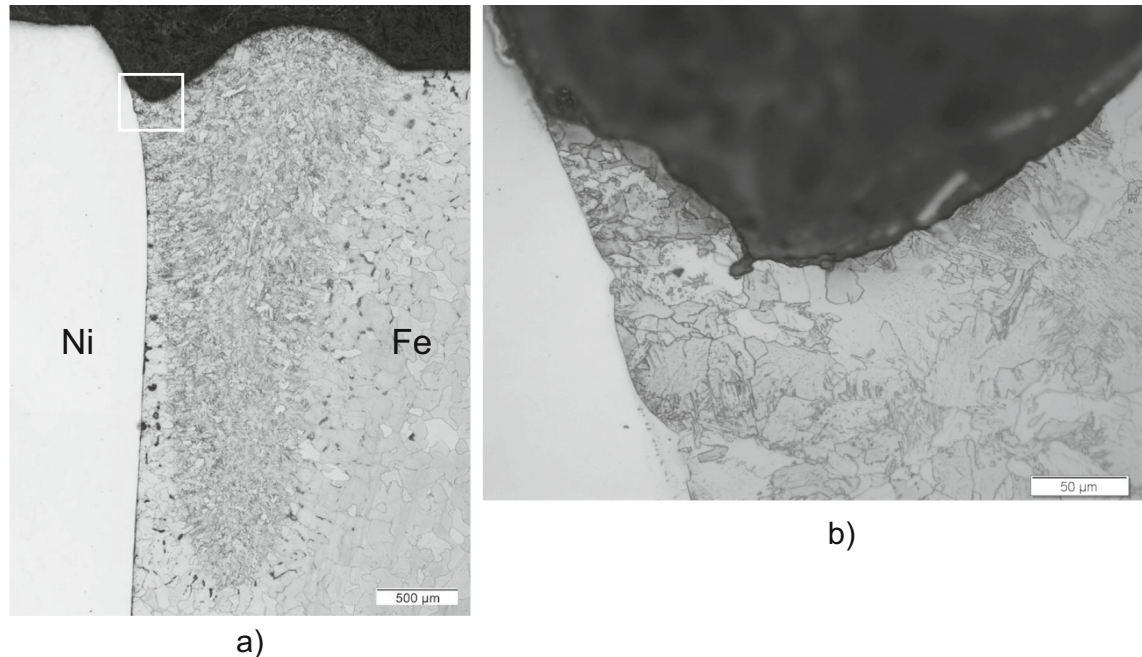


Fig. 4—(a) Weld section with a bulk fusion zone composition of  $> 99$  wt pct Fe. (b) Detail shows top of weld where the weld metal bridges over to the nickel substrate.

because the dominant parameter that controls the half-penetration width is the effective beam width, or the width of the electron beam combined with the amplitude of the deflection.

Figure 3(b) shows that the weld top width decreases as iron content in the bulk fusion zone increases. The sharp increase in weld top width observed at high iron content (above 94 wt pct Fe) is likely due to the mismatch in the working height of the two plates. As the weld progresses entirely into the iron, the molten metal bridges over to the nickel base plate, increasing the measured top width. An example of this is shown in Figure 4. It can also be seen that this results in a change in the slope of the weld crown as the weld begins to sag toward the nickel interface (also shown in Figure 3(e)). The increase in fusion zone area at high iron content shown in Figure 3(d) is directly related to the increase in weld top width. Beam deflection does not influence the weld geometry measurements due to the high frequency used in this study.<sup>[18]</sup>

### B. Composition Transition Zone

The width of the transition zone was determined based on compositional line scan data from EDS (see Figure 2(b)). This width was measured as the range of

compositions between the base metal and the bulk fusion zone composition. Figure 5 shows examples of line scans across the transition zone at the nickel and iron interfaces in a cross-section with a bulk fusion zone composition of 76.9 wt pct Fe. The width of the transition zone was measured as the distance between the base metal and where the fusion zone composition became largely uniform. Figure 5 shows a plot of the transition zone width as a function of bulk fusion zone composition (in wt pct Fe). The transition zone width increases at a larger composition gradient between the base metal and the fusion zone. As the compositional difference increases, the transition zone must expand in width to allow for transition due to the finite amount of solubility between iron and nickel.

It was also found that the transition zone was wider on the interface with the nickel work piece as compared to the side with the iron work piece. This difference in transition zone width is attributed to the melting temperatures of the two materials and the beam deflection. Pure iron melts at 1536 °C, whereas pure nickel melts at 1455 °C.<sup>[26]</sup> This 80 °C difference would result in the nickel interface solidifying at lower temperatures and thus enables the growth of the transition zone. Assuming the temperature gradient is similar throughout the weld, the area of the weld near the nickel

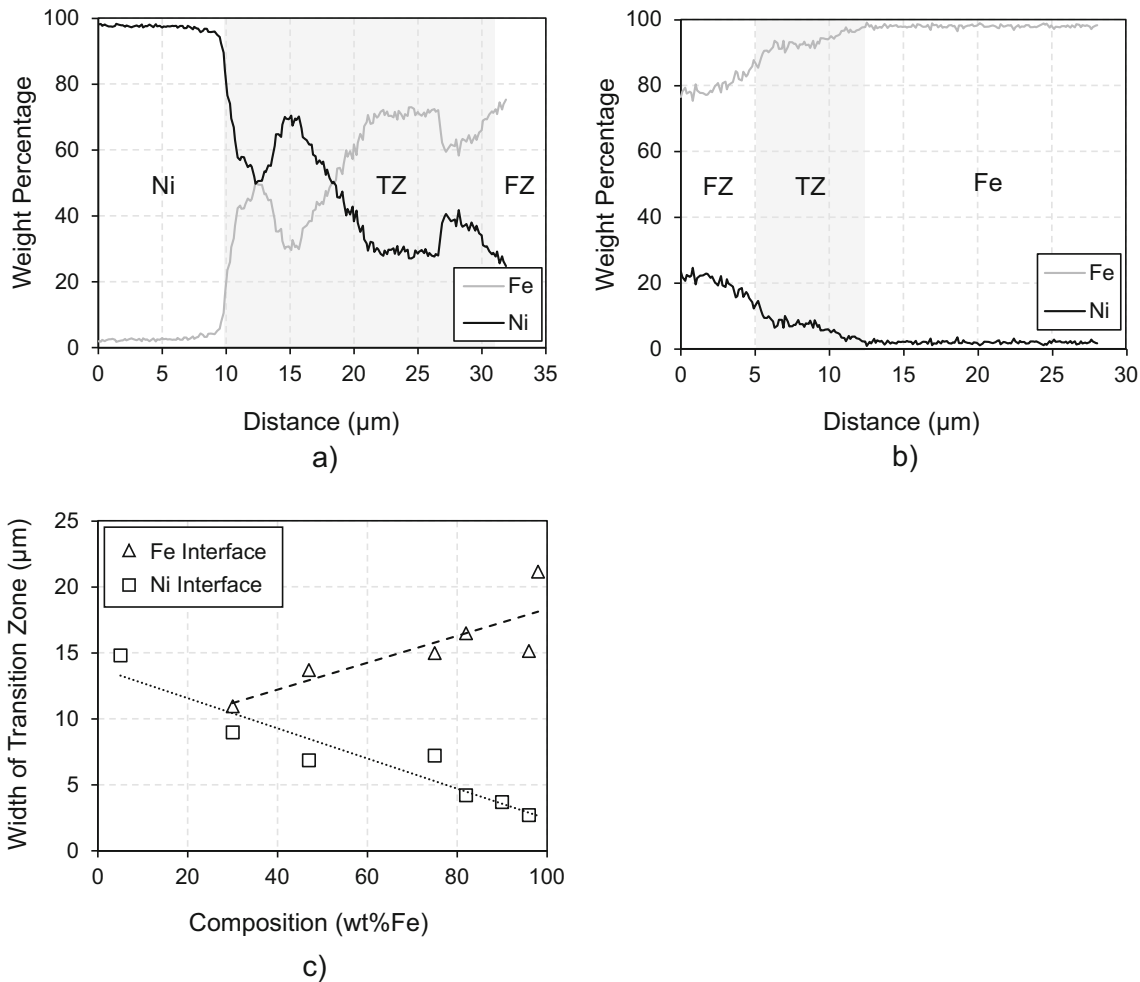


Fig. 5—Composition gradient across the transition zone (TZ) at the (a) nickel interface and (b) iron interface in weld section with 76.9 wt pct Fe bulk fusion zone (FZ) composition. Note that at the nickel interface, there are variations in transition zone composition due to iron-rich swirls. (c) Width of the transition zone toward the iron and nickel interface as a function of bulk fusion zone composition.

interface is liquid for longer times. Another thing to note is the large solubility of iron into nickel at temperatures near the melting point. There is a much smaller solubility of nickel into iron (which is delta ferrite at high temperatures) without a phase change. This may be another reason why the transition zone on the nickel interface is wider as compared to at the iron interface. The beam deflection allowed for more mixing and thus a narrower transition zone.

This argument considers diffusion in the liquid metal. Solid-state diffusion effects were thought to be minimal due to high calculated cooling rates. As the temperature drops rapidly, near the interface, so does the diffusion coefficient. Although the cooling rate will vary locally, an average was estimated using the cell spacing at the interface. An average of 10 measurements of the cell spacing at the nickel interface was measured as  $1.6 \mu\text{m}$  with a standard deviation of 0.3 and at the iron interface was measured as  $2.0 \mu\text{m}$  with a standard deviation of 0.3. The local cooling rate was calculated using the following formula derived by Katayama and Matsunawa<sup>[28]</sup>:

$$\lambda = 80(\varepsilon)^{-0.33},$$

where  $\lambda$  is the cell spacing and  $\varepsilon$  is the cooling rate. It is important to note that this relationship is valid for Type 310 stainless steel which has approximately 55 wt pct Fe, as well as large additions of Ni and Cr. Thus, the cooling rate was only estimated using the cell spacing at the interface in the cross-section with a bulk fusion zone composition of 54.7 wt pct Fe. This cooling rate was assumed relatively constant in the keyhole at each interface for this composition. It should be noted that beam deflection is not accounted for when using this equation. The calculated cooling rates were  $1.28 \times 10^6 \text{ }^\circ\text{C/s}$  at the nickel interface and  $7.15 \times 10^5 \text{ }^\circ\text{C/s}$  at the iron interface. Other literature has observed cooling rates for electron beam welds under similar conditions on the order of  $10^4 \text{ }^\circ\text{C/s}$  for cell spacings measured in the center of the weld and on the order of  $10^6 \text{ }^\circ\text{C/s}$  for cell spacings made at the fusion boundary,<sup>[29]</sup> which is in line with the present results. Although this is only considered for one bulk fusion zone composition, the order of magnitude of these

cooling rates are fast enough to assume no solid-state diffusion throughout the weld.

### C. Fusion Zone Microstructure

Optical microscopy imaging showed swirls of material from the base metal into the fusion zone, which have been observed in prior literature and were attributed to solidification prior to complete mixing.<sup>[13,30]</sup> The formation of swirls was further facilitated in this work by the use of beam deflection in a circular pattern, which swept material into the fusion zone. Examples of both types of swirls are shown in Figure 6. The degree of etching using 2 pct Nital and coloration of the fusion zone, as well as EDS compositional maps were used to illustrate the fusion zone swirls.

Evidence of a cellular solidification substructure was observed in weld cross-sections with a bulk fusion zone composition ranging from 4.0 to 94.3 wt pct Fe, indicating primary weld solidification as austenite (fcc). Figure 7 shows the evidence of austenite solidification substructure in the cross-section with 94.3 wt pct Fe bulk fusion zone composition. The solidification substructure is generally difficult to image in welds that solidify as primary ferrite due to the high diffusion rates in the bcc ferrite phase. Diffusion will eliminate compositional gradients in the intercellular regions quickly, so no substructure is observed in sections that solidified as primary ferrite. Saeid<sup>[31]</sup> found that the interdiffusion coefficient in Fe–Cr–Ni alloys at 1100 °C was  $1.13 \times 10^{-13} \text{ m}^2/\text{s}$  for nickel into ferrite, and  $1.15 \times 10^{-15} \text{ m}^2/\text{s}$  for nickel into austenite. In iron and steel systems, any residual substructure will be further obscured by subsequent phase transformations.

Austenitic solidification, as opposed to ferritic solidification, is of interest because it has a higher susceptibility to solidification cracking.<sup>[32,33]</sup> The change in solidification microstructure was predicted using a binary Ni–Fe equilibrium phase diagram calculated using the TCFE11: Steels/Fe-Alloys v11.0 database in Thermo-Calc<sup>®</sup> 2022b.<sup>[34]</sup> The phase diagram was calculated for vacuum conditions of  $3 \times 10^{-4}$  torr ( $3.9 \times 10^{-7}$  atm). The Fe-rich corner is shown in Figure 8 to focus on the region where the solidification behavior changes. Based on this portion of the phase diagram, the solidification sequence as a function of bulk fusion zone composition is summarized in Table IV. The modeled solidification sequences guided analysis and characterization of the solidified microstructure.

The predictions indicate that bulk fusion zone compositions up to 95.2 wt pct Fe will solidify as austenite. The primary solidification mode will be ferrite above 95.2 wt pct Fe. Figures 7, 9, and 10 show experimental evidence of austenitic solidification substructure in welds up to 94.3 wt pct Fe bulk fusion zone composition. There was no evidence of substructure in a weld cross-section with 96.0 wt pct Fe bulk fusion zone composition. The solidification behavior as seen from metallographic examination agrees reasonably well with what is predicted by the thermodynamic calculations.

There was a distinct shift in the etching characteristics of fusion zone microstructure in weld cross-sections with a bulk fusion zone composition 76.9 wt pct Fe as shown in Figures 9 and 10. The cross-sections with a high Fe content could be etched with 2 pct Nital. At lower Fe levels, it was necessary to etch with Kalling's 2 reagent to reveal the fusion zone microstructure. Figure 9 shows macrographs and the fusion zone microstructure at 4.0

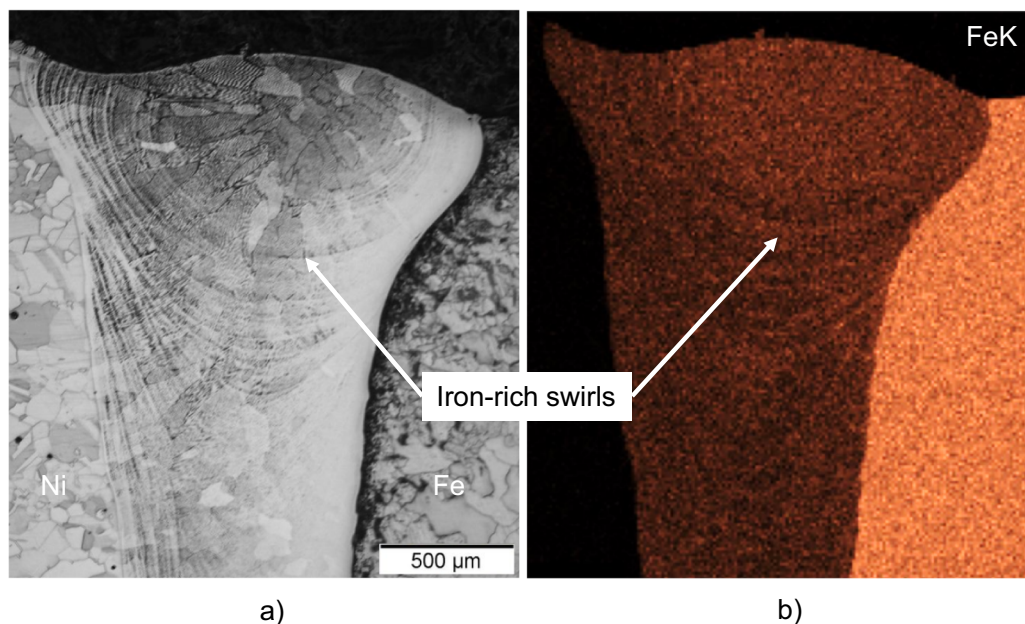


Fig. 6—Evidence of swirls in the fusion zone microstructure: (a) etched optical micrograph, and (b) EDS map for Fe. A cross-section with 30.3 wt pct Fe in the bulk fusion zone composition is shown.



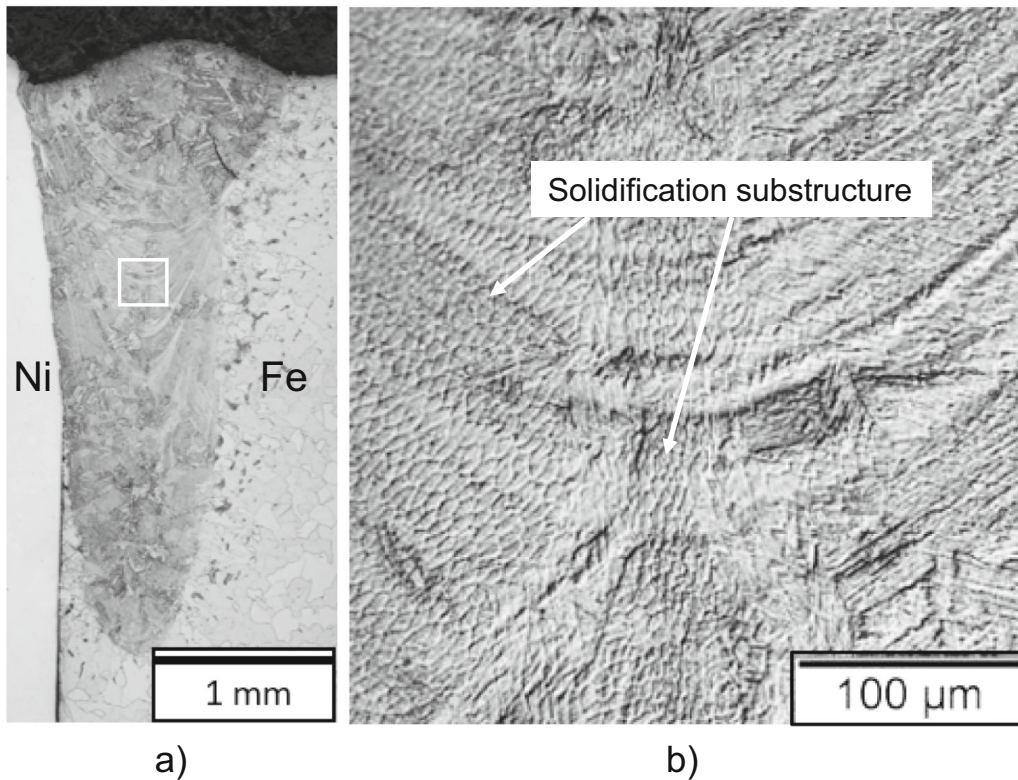


Fig. 7—Evidence of austenite solidification substructure. (a) Macrograph and (b) corresponding micrograph for the weld cross-section with 94.3 wt pct Fe bulk fusion zone composition. The substructure was made more evident by use of a differential interference contrast (DIC) filter in the light optical microscope.

wt pct Fe to 62.1 wt pct Fe bulk fusion zone composition. The substructure etched more effectively as the proportion of Fe in the fusion zone increased. At lower Fe compositions, the nickel interface fusion boundary was more difficult to distinguish.

Figure 10 shows weld cross-sections with 76.9 wt pct Fe to 98.2 wt pct Fe in the bulk fusion zone composition. These Fe-rich cross-sections etched more effectively and revealed greater detail in the fusion zone microstructure than the Ni-rich cross-sections. Some degree of etching was achieved using 2 pct Nital, even while displaying evidence of cellular substructure. Similar substructure morphologies have been reported in steels that contain a large amount of nickel as an alloying addition,<sup>[35–38]</sup> most likely due to the partitioning of Ni to the intercellular regions during solidification. The partition coefficient ( $k$ ) was calculated from the thermodynamic model using the equation:

$$k = \frac{C_s}{C_L},$$

where  $C_s$  is the composition of the solid phase and  $C_L$  is the composition of the liquid phase. When considering the residual elements found in the actual composition of the plate material (refer to Table I), utilizing a pseudo-binary phase diagram gives an average  $k$  value of 0.78. Based on SEM/EDS line scan data over a set of 10 cells in the section with 76.9 wt pct Fe, the  $k$  value was found to be 0.81 with a standard deviation of 0.026.

The composition of the solid was taken to be the composition at the center of the cell and the composition of the liquid was taken to be the composition in the intercellular region. With the high cooling rates experienced in EBW, the partitioning that occurs during solidification is maintained since interdiffusion is suppressed. Similar findings have been observed in splat cooling, and the partitioning is attributed to the degree of undercooling and fast cooling rates.<sup>[36]</sup> This partitioning is also maintained despite the solid-state transformation to ferrite at lower temperatures (see Figure 1). This partitioning effect has been described by others.<sup>[35–37]</sup>

In EBSD analysis, the fusion zone microstructure is indexed as fully fcc in weld cross-sections with a bulk fusion zone composition of up to 54.7 wt pct Fe (Figure 11(a)), whereas cross-sections with 84.0 wt pct Fe and above are indexed as bcc (Figure 11(d)). In two weld cross-sections, both fcc and bcc regions were observed, where the bcc phase had a higher Fe content as compared to the fcc. At 65.5 wt pct Fe in the bulk fusion one composition, approximately 39 pct bcc was observed (Figure 11(b)). At 76.9 wt pct Fe, approximately 88 pct bcc was observed (Figure 11(c)). These two weld cross-sections also displayed fcc structure in some of the intercellular regions of the swirls due to the microsegregation of nickel to these regions, as shown in Figure 11. Relating these results to the bulk fusion zone composition, the mixed fcc/bcc region was calculated to be between 56.4 wt pct Fe and 79.7 wt pct Fe. The bcc

phase in Figure 11 is likely a mixture of martensite and ferrite.

A solid-state transformation from austenite occurs in the Fe-rich portion of the phase diagram, as shown in Figure 1. While the equilibrium phase is ferrite, under rapid cooling conditions, the transformation product is martensite.<sup>[39]</sup> Although this weld has a low-carbon content, martensite can still form in an Fe–Ni system due to a driving force for the fcc phase to transform to the bcc phase at a cooling rate where diffusion is not possible.<sup>[40,41]</sup> Fe–Ni martensite is different from Fe–C martensite in that it is typically softer due to less lattice strain and a much lower dislocation density. Using EBSD, it is difficult to distinguish between ferrite and martensite, so they cannot be clearly differentiated when producing phase maps. However, a structure difference can be seen in the inverse pole figure (IPF) maps. Figure 12 shows the structure differences between a weld cross-section with 84 wt pct Fe in the bulk fusion zone composition and a cross-section at the end of the weld that has > 99 wt pct Fe in the bulk fusion zone composition. Typical lath martensite morphologies in

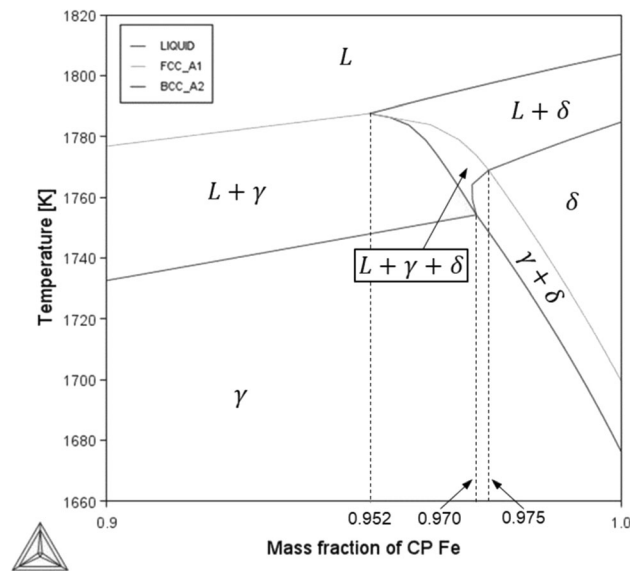


Fig. 8—Solidification region of interest for the Ni–Fe binary equilibrium phase diagram at  $3 \times 10^{-4}$  torr. Calculated using Thermo-Calc<sup>®</sup> Iron and Steel Database (TCFE11: Steels/Fe-Alloys v11.0).

the form of parallel arrangements of lath-shaped grains can be seen in the sections with nickel content (Figure 12(a)), whereas the section with essentially 100 pct Fe shows polygonal ferrite (Figure 12(b)). To determine if a shift from martensite to ferrite occurs at high Fe content, hardness measurements were performed. Hardness indents were made at the top, middle, and bottom on the weld cross-sections, and an average was taken to represent the hardness of the entire fusion zone. Figure 13 shows the hardness data as a function of wt pct Fe in the bulk fusion zone composition.

The weld cross-sections with a bulk fusion zone composition of 54.7 and 65.5 wt pct Fe consisted primarily of austenite resulting in a low hardness reading of 130 to 140 HVN. As the amount of bcc in the fusion zone microstructure increases at higher wt pct Fe, the hardness also increases (Figure 13). The hardness of weld cross-section containing martensite was between 216 and 305 HVN. The hardness of Fe–Ni martensite within a compositions range of 64 to 100 wt pct Fe has been shown to be approximately 225 to 275 HVN.<sup>[39]</sup> The hardness of martensite in the Fe–Ni system has been shown to be significantly lower than the hardness of Fe–C martensite due to the much lower effect of Ni to strengthen the martensite due to smaller lattice strains, the much lower dislocation density of Fe–Ni martensite, and the reduced effect of packet and block size on Fe–Ni martensite strength.<sup>[42,43]</sup> The weld cross-section with 76.9 wt pct Fe in the bulk fusion zone composition showed an increase in hardness, but also a large degree of scatter. This is due to the hardness indents being made in areas containing both fcc and bcc phases, as determined by EBSD. This scatter was significantly reduced as the microstructure became single-phase bcc. There is an increase in hardness to a peak of approximately 305 HV at 90.0 wt pct Fe in the bulk fusion zone composition, confirming the presence of martensite. Above this level, as the amount of nickel decreases, ferrite predominates over martensite, as indicated by the drop in hardness toward 100 wt pct Fe.

#### IV. CONCLUSIONS

In this work, a single weld of variable composition was made between commercially pure iron and nickel in order to investigate the effect of fusion zone composition

**Table IV. Effect of Bulk Fusion Zone Composition on Solidification Sequence, as Predicted by the Thermo-Calc<sup>®</sup> Calculated Ni–Fe Equilibrium Phase Diagram**

Composition (Wt Pct Fe)	Solidification Sequence
0 to 95.2*	$L \rightarrow L + \gamma \rightarrow \gamma$
95.2 to 97.0	$L \rightarrow L + \delta \rightarrow L + \delta + \gamma \rightarrow L + \gamma \rightarrow \gamma$
97.0 (Monovariant Point)	$L \rightarrow L + \delta \rightarrow L + \delta + \gamma \rightarrow \gamma$
97.0 to 97.5	$L \rightarrow L + \delta \rightarrow L + \delta + \gamma \rightarrow \delta + \gamma \rightarrow \gamma$
97.5	$L \rightarrow L + \delta \rightarrow \delta + \gamma \rightarrow \gamma$
97.5 to 100	$L \rightarrow L + \delta \rightarrow \delta \rightarrow \delta + \gamma \rightarrow \gamma$

\*Primary austenite solidification predicted.

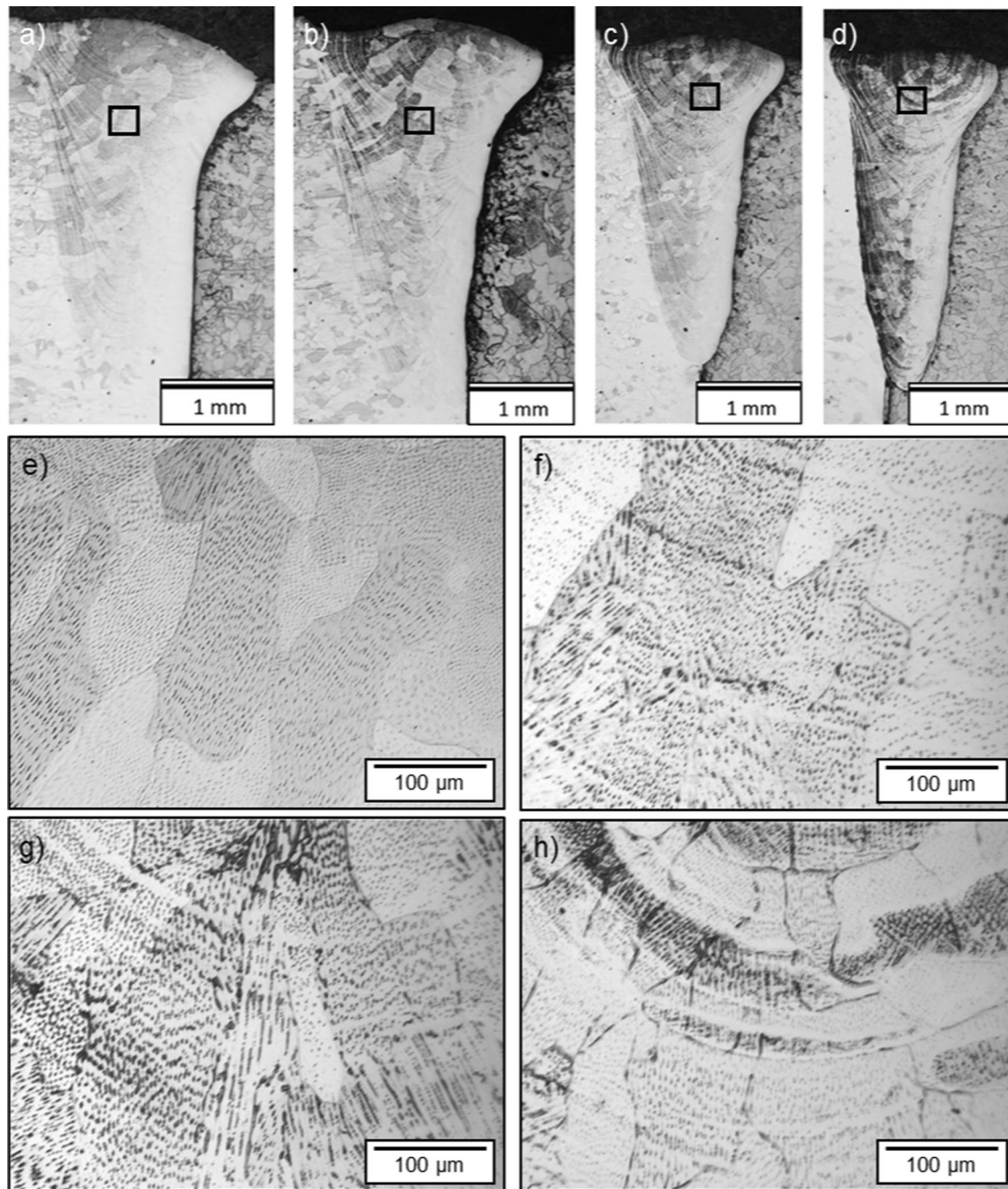


Fig. 9—Macrographs and corresponding micrographs of fusion zone microstructure for weld cross-sections with (a, e) 4.0 wt pct Fe, (b, f) 16.4 wt pct Fe, (c, g) 42.5 wt pct Fe, and (d, h) 65.5 wt pct Fe in the bulk fusion zone composition.

on the size of the transition region, weld geometry, solidification mode, and resultant microstructure. The following observations were made:

1. The composition transition zone increased in width as the difference in composition between the fusion zone and the base material increased. This occurred to accommodate the larger compositional gradient. Solid-state diffusion was minimal.
2. The width of the transition region toward the nickel substrate is larger than that at the interface toward the iron substrate.
3. Fusion zone geometries showed a deeper weld penetration with higher iron content in the bulk fusion zone composition, indicating a dependence on the vapor pressure, density, and surface tension of the material. Half-penetration width and fusion zone area were relatively constant.

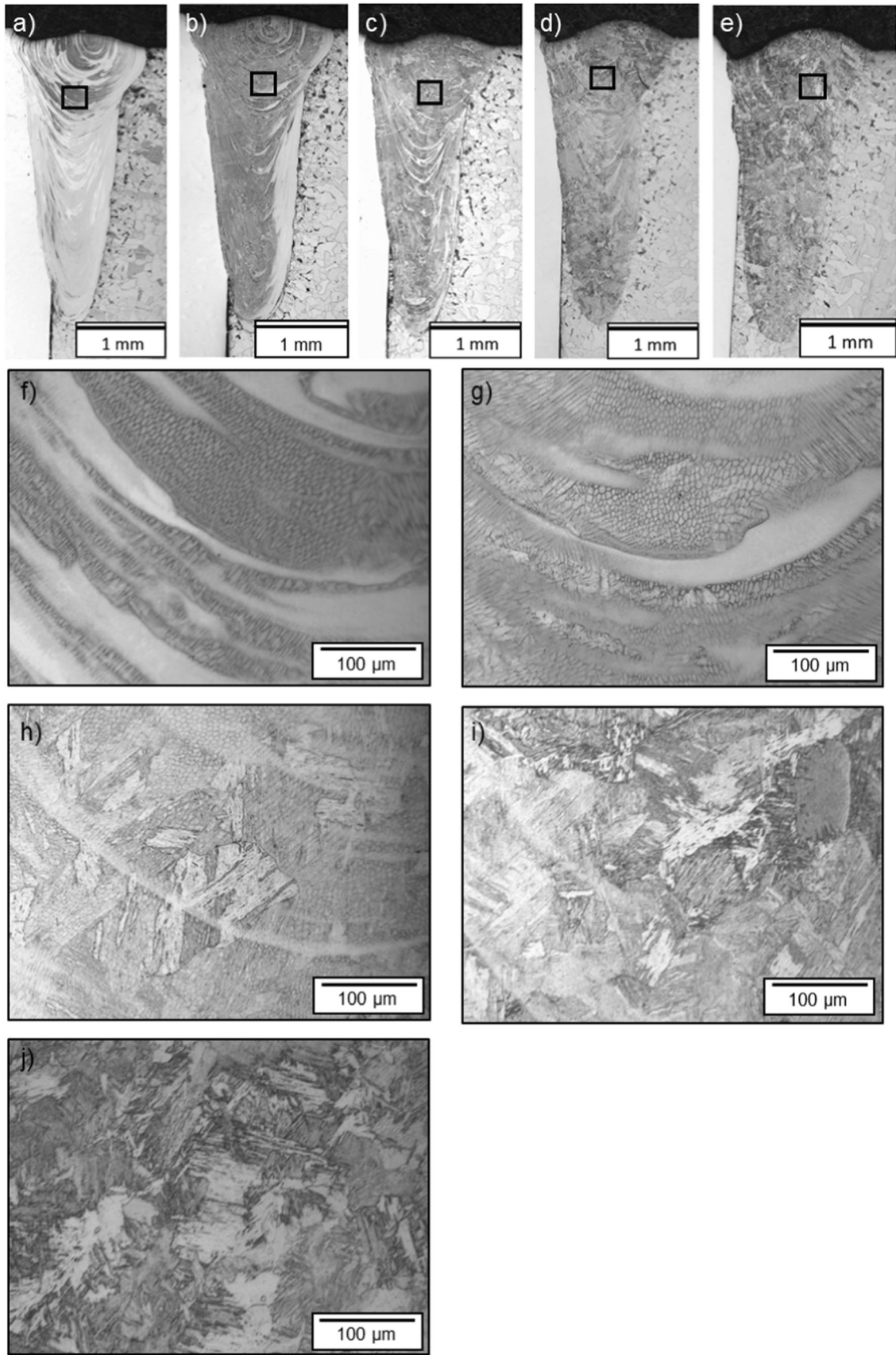


Fig. 10—Macrographs and corresponding micrographs of fusion zone microstructure for weld cross-sections with (a, f) 76.9 wt pct Fe, (b, g) 84.0 wt pct Fe, (c, h) 90.4 wt pct Fe, (d, i) 94.3 wt pct Fe, and (e, j) 98.0 wt pct Fe in the bulk fusion zone composition.

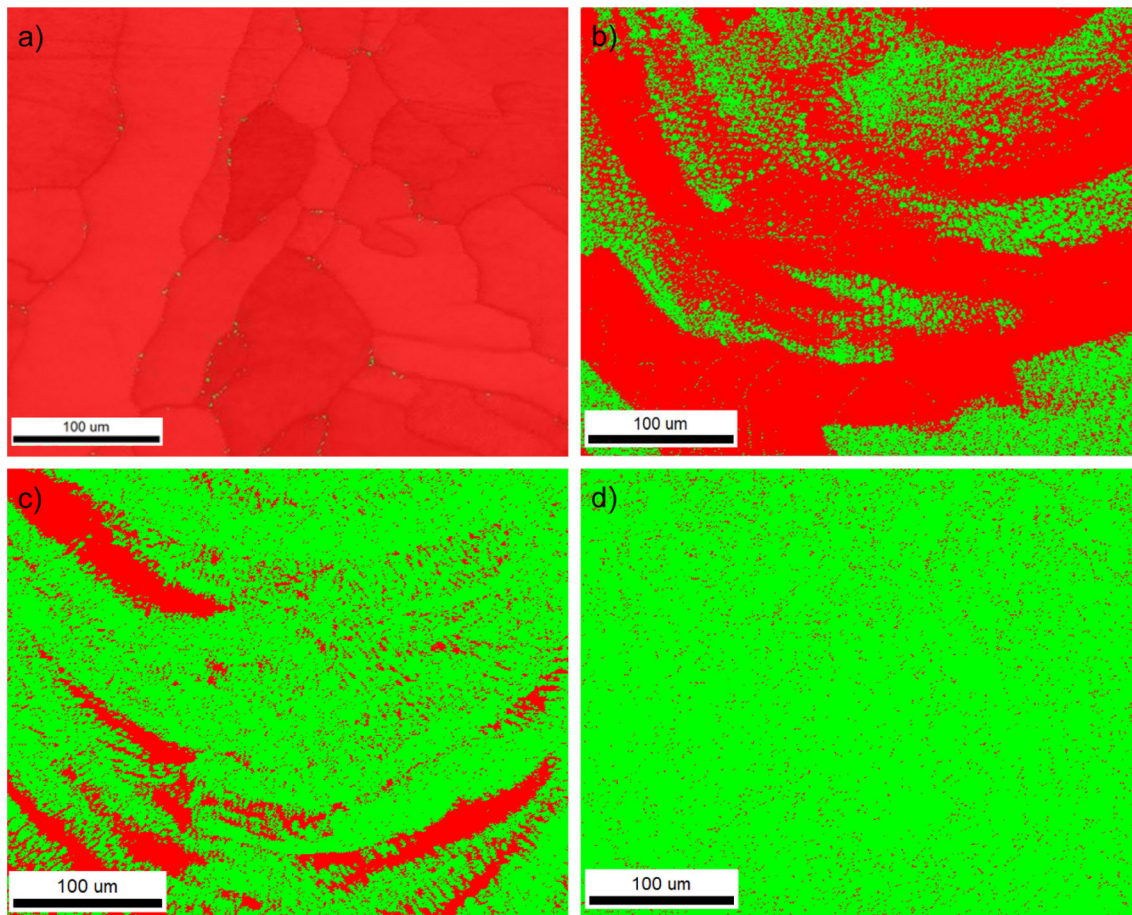


Fig. 11—EBSD maps from the fusion zone microstructure of weld cross-sections with (a) 54.7 wt pct Fe, (b) 65.5 wt pct Fe, (c) 76.9 wt pct Fe, and (d) 84.0 wt pct Fe in the bulk fusion zone composition. Red indicates regions indexed as fcc and green indicates regions indexed as bcc (Color figure online).

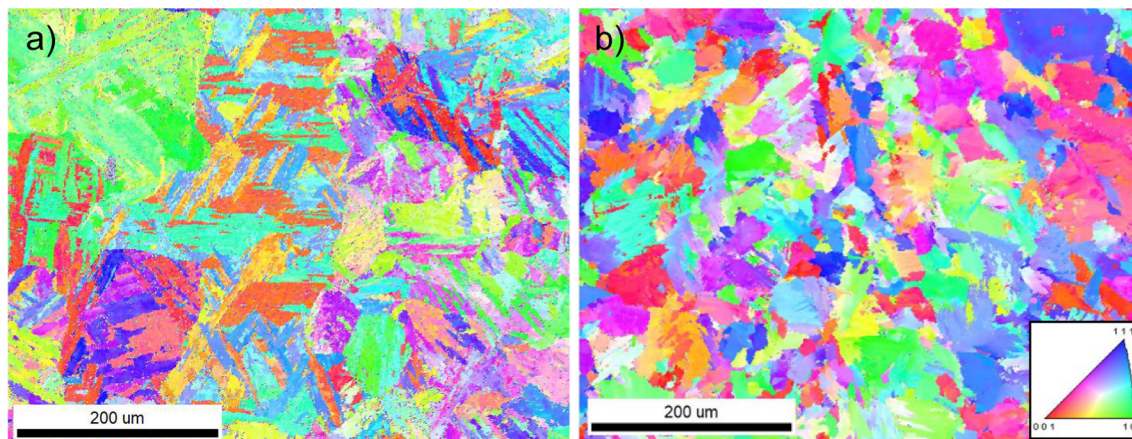


Fig. 12—Inverse pole figure maps of the fusion zone microstructure for weld cross-sections with (a) 84.0 wt pct Fe and (b) > 99.0 wt pct Fe in the bulk fusion zone composition (Color figure online).

4. Evidence of solidification substructure was observed in the majority of weld cross-sections up to 94.3 wt pct Fe in the bulk fusion zone composition.
5. Substructure is evident in weld sections that solidified as austenite. This is the result of local nickel

segregation to sub-grain boundaries at the end of solidification (coring effect in non-equilibrium solidification) which is not altered by solid-state diffusion. Substructure was not observed in weld sections that solidified as ferrite.

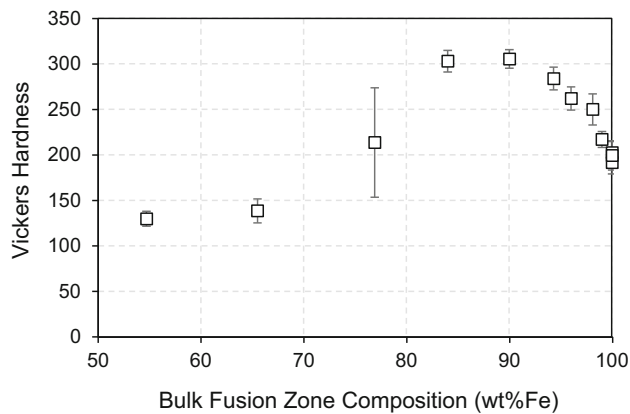


Fig. 13—Vickers hardness as a function of wt pct Fe in the bulk fusion zone composition.

- The fusion zone was indexed using EBSD as predominantly fcc in weld cross-sections up to 54.7 wt pct Fe in the bulk fusion zone composition. Cross-sections with 65.5 and 75.6 wt pct Fe contained both bcc and fcc. Cross-sections with over 84.0 wt pct Fe indexed only as bcc.
- Martensite formed in weld cross-sections which indexed as bcc and contained iron in the range from 76.9 to 98.1 wt pct in the bulk fusion zone composition. The presence of martensite was confirmed using EBSD and hardness data.

These findings are significant when considering the role of weld composition. Important aspects to consider when looking at any weld include weld geometry and microstructure. It is also important to consider cracking susceptibility, which is influenced by the solidification sequence and, in dissimilar metal welds, the transition zone. These results present a high-throughput approach to analyze a weld in each of these areas for an application that may be restrictive in composition or dilution limits.

## V. FUTURE WORK

In further investigations, the authors will aim to study the nucleation and growth at the fusion boundary in this Fe–Ni weld, and the evolution of microstructure resulting from dissimilar crystallographic nucleation, *i.e.*, fcc nucleation from a bcc substrate and bcc nucleation from an fcc substrate.

## ACKNOWLEDGMENTS

The authors would like to acknowledge the Manufacturing and Materials Joining Innovation Center (Ma<sup>2</sup>JIC) funded through the National Science Foundation Industry University Cooperative Research Center program (IUCRC) for its support in this research (award number 2052747). The authors would also like to thank Los Alamos National Laboratory for

experimental and financial support in this project, specifically Dr. David Tung and Dr. Matthew Johnson for their mentorship. Electron microscopy was performed at the Center for Electron Microscopy and Analysis (CEMAS) at The Ohio State University. Finally, the authors would like to thank undergraduate researcher Jacob Popham, who assisted with the metallographic preparation of these samples.

## OPEN ACCESS

This article is licensed under a Creative Commons Attribution 4.0 International License, which permits use, sharing, adaptation, distribution and reproduction in any medium or format, as long as you give appropriate credit to the original author(s) and the source, provide a link to the Creative Commons licence, and indicate if changes were made. The images or other third party material in this article are included in the article's Creative Commons licence, unless indicated otherwise in a credit line to the material. If material is not included in the article's Creative Commons licence and your intended use is not permitted by statutory regulation or exceeds the permitted use, you will need to obtain permission directly from the copyright holder. To view a copy of this licence, visit <http://creativecommons.org/licenses/by/4.0/>.

## COMPETING INTERESTS

The authors declare that they have no known competing financial interests or personal relationships that could have appeared to influence the work reported in this paper.

## REFERENCES

- A.V. Thakur: *Maer's Mit Pune J.*, 1992, vol. 1(1), pp. 75–80.
- T. Patterson, J. Hochanadel, S. Sutton, B. Pantan, and J. Lippold: *Weld World*, 2021, vol. 65(7), 1235–1306. <https://doi.org/10.1007/s40194-021-01116-0>.
- R. Rai, P. Burgardt, J.O. Milewski, T.J. Lienert, and T. Debroy: *J. Phys. D Appl. Phys.*, 2009, vol. 42(2), pp. 1–2. <https://doi.org/10.1088/0022-3727/42/2/025503>.
- P. Burgardt and C. Heiple: *Weld J.*, 1992, vol. 71(9), pp. 341s–47s.
- W.H. Giedt and L.N. Tallerico: *Weld J.*, 1988, vol. 67(12), pp. 299s–305s.
- C.W. Weidner and L.E. Shuler: *Weld J.*, 1973, vol. 52(3), 114s–119s.
- P.W. Hochanadel, P. Burgardt, J.W. Elmer, D. Kautz, and D. Dean: *Some Physics Fundamentals of High Energy Density Welding*, Los Alamos National Laboratory, Los Alamos, 2021.
- J.E. Hochanadel, T. Patterson, J.C. Lippold, B. Pantan, M.Q. Johnson, and D.C. Tung: *Weld World*, 2021, vol. 65(5), pp. 1007–1014. <https://doi.org/10.1007/s40194-020-01046-3>.
- J. Kar, S.K. Roy, and G.G. Roy: *J. Mater. Process. Technol.*, 2016, vol. 233, pp. 174–85. <https://doi.org/10.1016/j.jmatprotec.2016.03.001>.
- C. Wiednig, C. Lochbichler, N. Enzinger, C. Beal, and C. Sommitsch: *Procedia Eng.*, 2014. <https://doi.org/10.1016/j.proeng.2014.11.027>.

11. F. Franchini: *Weld. Int.*, 1993, vol. 7(3), pp. 206–210. <https://doi.org/10.1080/09507119309548374>.
12. T.V. Olshanskaya, G.L. Permyakov, V.Y. Belenkiy, and D.N. Trushnikov: *Mod. Appl. Sci.*, 2015, vol. 9(6), pp. 296–309. <https://doi.org/10.5539/mas.v9n6p296>.
13. R. Buntain: PhD Dissertation, The Ohio State University, 2020.
14. J.N. Dupont and R.E. Mizia, *Review of Dissimilar Metal Welding for the NGNP Helical-Coil Steam Generator*, Idaho National Laboratory, Idaho Falls, 2010.
15. R.E. Avery: *Pay Attention to Dissimilar-Metal Welds*, Nickel Development Institute, Toronto, 1991.
16. H.M.E. Okamoto, M.E. Schlesinger, and E.M. Mueller, eds., *ASM Handbook, Volume 3: Alloy Phase Diagrams*, vol. 3. ASM International, Materials Park, 2016.
17. J. Rinne, O. Seffer, S. Nothdurft, J. Hermsdorf, S. Kaierle, and L. Overmeyer: *J. Mater. Process. Technol.*, 2021, vol. 296, pp. 1–1. <https://doi.org/10.1016/j.jmatprotec.2021.117178>.
18. D. Kaisheva, V. Angelov, and P. Petrov: *Can. J. Phys.*, 2019, vol. 97(10), pp. 1140–46. <https://doi.org/10.1139/cjcp-2018-0495>.
19. J.I. Goldstein, R.E. Hanneman, and R.E. Ogilvie: *Trans. Met. Soc. AIME*, 1965, vol. 233(4), pp. 812–20.
20. G. Krauss: *Mater. Sci. Eng.*, 1999, vols. 273–275, pp. 40–57.
21. G.B. Olson and M. Cohen: *Metall. Trans. A*, 1976, vol. 7A, pp. 1905–914.
22. A. Block-Bolten and T.W. Eagar: *Metall. Trans. B*, 1984, vol. 15B, pp. 461–69.
23. X. He, T. DeRoy, and P.W. Fuerschbach: *J. Phys. D Appl. Phys.*, 2003, vol. 36, pp. 3079–88.
24. J. F. Kerridge, M. S. Matthews, and A. Meibom: in *Proc. NIRP Symp. Antarct. Meteorites*, JGR Planet, 2004, pp. 1–2.
25. J. Brillo and I. Egry: *J. Mater. Sci.*, 2005, vol. 40, pp. 2213–16.
26. Z. Sun and J.C. Ion: *J. Mater. Sci.*, 1995, vol. 30, pp. 4205–214.
27. J. Brillo and I. Egry: *Int. J. Thermophys.*, 2003, vol. 24(4), pp. 1155–70.
28. S. Katayama and A. Matsunawa: in *ICALEO® '84: Proceedings of the Laser Materials Processing Symposium*, 1984, pp. 60–67. [http://pubs.aip.org/liacp/proceedings-pdf/ICALEO/1984/60/9026767/60\\_1\\_online.pdf](http://pubs.aip.org/liacp/proceedings-pdf/ICALEO/1984/60/9026767/60_1_online.pdf).
29. J. W. Elmer, Dissertation, Massachusetts Institute of Technology, 1988.
30. T. Soysal, S. Kou, D. Tat, and T. Pasang: *Acta Mater.*, 2016, vol. 110, pp. 149–60. <https://doi.org/10.1016/j.actamat.2016.03.004>.
31. M. Saied, Thesis, Universite Grenoble Alpes, 2016.
32. V. Kujanpaa, N. Suutala, T. Takalo, and T. Moisio: *Weld. Res. Int.*, 1979, vol. 9(2), pp. 55–76.
33. J.A. Brooks and A.W. Thompson: *Int. Mater. Rev.*, 1991, vol. 36(1), pp. 16–44. <https://doi.org/10.1179/imr.1991.36.1.16>.
34. “Thermo-Calc® version 2022b.Database: TCFE11: Steels/Fe-Alloys v11.0, 2022.
35. A.G. Dobbins, J.W. Koger, and T.M. Mustaleski: *Corrosion Testing Type HP 9-4-20-Steel*, Oak Ridge National Laboratory, Oak Ridge, 1979.
36. T.Z. Kattamis, W.F. Brower, and R. Mehrabian: *J. Cryst. Growth*, 1973, vol. 19, pp. 229–36.
37. S. Khodir, T. Shibayanagi, M. Takahashi, H. Abdel-Aleem, and K. Ikeuchi: *Mater. Des.*, 2014, vol. 60, pp. 391–400. <https://doi.org/10.1016/j.matdes.2014.03.056>.
38. A.M. El-Batahgy, A. Gumenyuk, S. Gook, and M. Rethmeier: *J. Mater. Process. Technol.*, 2018, vol. 261, pp. 193–201. <https://doi.org/10.1016/j.jmatprotec.2018.05.023>.
39. T. Zeng: *J. Alloys Compd.*, 2022, vol. 894, pp. 1–6. <https://doi.org/10.1016/j.jallcom.2017.08.285>.
40. L. Kaufman and M. Cohen: *Prog. Met. Phys.*, 1958, vol. 1, pp. 165–246.
41. L. Kaufman and M. Cohen: *J. Met.*, 1956, vol. 8, pp. 1393–401.
42. S. Takaki, K.-L. Ngo-Huynh, N. Nakada, and T. Tsuchiyama: *ISIJ Int.*, 2012, vol. 52(4), pp. 710–16.
43. S. Morito, J. Nishikawa, and T. Maki: *ISIJ Int.*, 2003, vol. 43(9), pp. 1475–77.

**Publisher's Note** Springer Nature remains neutral with regard to jurisdictional claims in published maps and institutional affiliations.